



HAL
open science

Statistical study of non-adiabatic energization and transport in Kelvin-Helmholtz vortices 2 at Mercury

**Key words: Mercury's magnetosphere,
Kelvin-Helmholtz instability, particle**

Sae Aizawa, Dominique C. Delcourt, Naoki Terada, Nicolas André

► **To cite this version:**

Sae Aizawa, Dominique C. Delcourt, Naoki Terada, Nicolas André. Statistical study of non-adiabatic energization and transport in Kelvin-Helmholtz vortices 2 at Mercury Key words: Mercury's magnetosphere, Kelvin-Helmholtz instability, particle. Planetary and Space Science, 2020, 193, pp.105079. 10.1016/j.pss.2020.105079 . hal-02550570v1

HAL Id: hal-02550570

<https://hal.science/hal-02550570v1>

Submitted on 22 Apr 2020 (v1), last revised 15 Nov 2020 (v2)

HAL is a multi-disciplinary open access archive for the deposit and dissemination of scientific research documents, whether they are published or not. The documents may come from teaching and research institutions in France or abroad, or from public or private research centers.

L'archive ouverte pluridisciplinaire **HAL**, est destinée au dépôt et à la diffusion de documents scientifiques de niveau recherche, publiés ou non, émanant des établissements d'enseignement et de recherche français ou étrangers, des laboratoires publics ou privés.

1 **Statistical study of non-adiabatic energization and transport in Kelvin-Helmholtz vortices**
2 **at Mercury**

3

4 Sae Aizawa[1][2], Dominique Delcourt[3], Naoki Terada[2], and Nicolas André[1]

5

6 *[1]Institut de Recherche en Astrophysique et Planétologie, CNRS-UPS-CNES, Toulouse,*
7 *France*

8 *[2]Department of Geophysics, Graduate School of Science, Tohoku University, Sendai, Japan*

9 *[3]Laboratoire de Physique et Chimie de l'environnement et l'espace, Université Orleans-CNRS,*
10 *Orleans, France*

11

12 **Key words: Mercury's magnetosphere, Kelvin-Helmholtz instability, particle**
13 **acceleration, transport, planetary ion**

14

15 **Abstract.** Non-adiabatic energization and transport of planetary ions in the vicinity of Kelvin-
16 Helmholtz (KH) vortices at Mercury are statistically investigated using a
17 magnetohydrodynamic model combined with a test particle tracing technique. The
18 measurements from the MErcury Surface, Space ENvironment, GEOchemistry, and Ranging
19 spacecraft show the signature of KH waves in the magnetospheric flanks, especially on the
20 duskside. We examine here the energization and transport of heavy ions of planetary origin
21 such as Na^+ associated with the growth of the KH instability on both the dawn and dusk sides
22 of the magnetosphere, and for both northward and southward interplanetary magnetic field
23 configurations. We find that in all cases picked up planetary ions in the magnetosphere can be
24 accelerated non-adiabatically with a level of acceleration larger on the dawnside. The transport
25 of ions is controlled by the convection electric field in the magnetosheath. The planetary ions

26 picked up in the duskside magnetosphere stagnate inside the magnetosphere where the KH
27 waves have been mainly observed at Mercury and, hence, are not expected to escape. The
28 present study indicates that these energized ions may likely stay inside the magnetosphere and
29 sputter the planetary surface on the duskside preferentially, being the source of secondary
30 neutrals from the planetary surface.

32 **1. Introduction**

33 The MErcury Surface, Space ENvironment, GEochemistry, and Ranging (MESSENGER)
34 spacecraft, the first orbiter around Mercury, was in orbit from March 11, 2011 until April 30,
35 2015. The many data collected provided in particular key information on the structure of the
36 magnetosphere as well as on the dynamics of the plasma environment around Mercury. A
37 number of plasma processes similar to the ones identified at Earth have been reported: magnetic
38 reconnection and Flux Transfer Events (FTE) at the magnetopause [Slavin et al., 2009, 2010b,
39 2014; DiBraccio et al., 2013; Imber et al., 2014], substorm-like dipolarization events in the
40 magnetotail [e.g., Sundberg et al., 2012a, Imber et al., 2017; Dewey et al., 2017, 2018], and
41 Kelvin-Helmholtz (KH) vortices in the magnetospheric flanks [Boardsen et al., 2010; Sundberg
42 et al., 2011, 2012b; Liljeblad et al., 2014, 2016; Gershman et al., 2015]. Moreover, the
43 MESSENGER data have shown evidence of heavy ions of planetary origin in several regions
44 of Mercury's magnetosphere, those resulting from the ionization of exospheric neutrals by solar
45 UV [Zurbuchen et al., 2011; Schriver et al., 2011a, b; Raines et al., 2011, 2013; DiBraccio et
46 al., 2013; Gershman et al., 2015]. These planetary ions can contribute to the mass loading and
47 structural stability of Mercury's environment, and can also drive original plasma processes.
48 Mercury, like Earth, has its own intrinsic magnetic field. Since this magnetic field is weaker
49 than the magnetic field of Earth, the size of Mercury's magnetosphere is relatively small. As a
50 result, the plasma processes at Mercury should occur faster, e.g., the Dungey plasma cycle at
51 Mercury lasts for a few minutes only while it lasts for a few hours at Earth [Siscoe et al., 1975;
52 Slavin et al., 2010a]. In addition, the heavy ions of planetary origin have a scale comparable to
53 the scale of plasma processes due to their large gyration motion. Under these circumstances,
54 the ion motion and the electromagnetic field variations within the magnetosphere are strongly
55 coupled and thus the plasma processes at Mercury are expected to be affected by these coupling.
56 The interactions between the planetary heavy ions and the variable electromagnetic fields at

57 Mercury have been investigated by various authors. In particular, Delcourt et al. (2003)
58 investigated how magnetic field variations affect essentially the ion motion. They showed that
59 a dipolarization in the magnetotail can accelerate ions non-adiabatically by violating the first
60 adiabatic invariant (the magnetic moment μ). Aizawa et al. (2018) further investigated how
61 sudden electric field variations - E burst – occurring during the development of the KH
62 instability can also lead to non-adiabatic acceleration of ions. They show how these accelerated
63 ions can effectively sputter the planetary surface and produce secondary neutrals and ions that
64 populate both the exosphere and magnetosphere of Mercury. In addition, Gingell et al. (2015)
65 revealed that the presence of heavy planetary ions can modify the growth of the KH instability,
66 which was previously reported by MESSENGER observations [Gershman et al., 2015]. The
67 KH instability is a macroscopic instability that occurs at several planets' magnetopause and
68 known to be an important process for mixing plasma of different origin under a particular
69 interplanetary magnetic field (IMF) configuration (e.g., northward for Earth and Mercury).
70 Indeed, when the instability fully developed, it forms large rolled-up KH vortices where
71 magnetic reconnection can occur.

72 In the present study, the non-adiabatic acceleration and related transport in both the
73 dawn and dusk flanks of the magnetosphere of Mercury during the development of the KH
74 instability are investigated in detail. Although Aizawa et al. (2018) already revealed that heavy
75 ions can be accelerated by this process, the configuration they used was restricted to the dawn
76 side of the magnetosphere. Since MESSENGER observations show that a strong dawn-dusk
77 asymmetry on the KH occurrence at Mercury exists [Liljeblad et al., 2014], it appears necessary
78 to extend the study of Aizawa et al. (2018) to the dusk side of the magnetosphere. The present
79 study focuses on the transport of ions due to the field variations and investigates in more details
80 the role of the convection electric field. In order to explore the dynamics of heavy ions, we
81 performed the same numerical method that Aizawa et al. (2018) conducted, launching single

82 particle trajectory computations in the KH field obtained by MHD simulations. In addition,
83 previous study considered only sodium ions whereas here we include other ions such as solar
84 wind plasma, oxygen and potassium planetary ions, and discuss from a statistical analysis the
85 dependence of the acceleration and transport of ions with their Larmor radius. In Section 2, we
86 introduce our modeling approach and initial settings used. We detail the results of our
87 simulations in Section 3 and discuss their interpretation in Section 4. Section 5 summarizes our
88 conclusions.

89

90 **2. Field Configuration and Overview of ion behavior**

91 In order to investigate the dynamics of heavy ions of planetary origin under realistic
92 conditions for Mercury, we adopt the same approach than the one used in Aizawa et al. (2018).
93 We trace the motion of particles in the KH field configurations obtained from MHD simulations.
94 A detailed description of the numerical scheme and conditions used can be found in Aizawa et
95 al. (2018). In the present study, quantitative and systematic calculations were performed in
96 configurations representative for both the dawn and dusk sides of Mercury's magnetosphere.
97 All parameters are carefully chosen from observational data when available. In addition, various
98 ion species, not only Na^+ but also O^+ , K^+ (heavy ions of planetary origin), H^+ , H_2^+ , (lighter
99 ions of planetary origin), and H^+ , He^{2+} (solar wind plasmas) are included in the present study,
100 as characterized by Zurbuchen et al. (2008). All ions are injected as picked up ions at given
101 times. The size of a simulation box in the x-direction, corresponding to the KH wavelength, is
102 set to exactly $1.5 R_M$ where R_M is Mercury radius, and the size in the y-direction is taken as 12
103 R_M with a spatial resolution of 32.2 km (114 x 909 grids). The thickness of the magnetopause
104 (boundary layer) is ~ 515 km (referred to $2a$ hereafter) as estimated in Gershman et al. (2015).
105 Ions are traced in the frame of the average motion of the KH wave, the periodical boundary
106 condition being set in the x-direction. All our parameter settings are summarized in Table 1.

107 The variations of all physical quantities across the magnetopause follow hyperbolic tangent
108 profiles.

109 Although MESSENGER observations did not enable us to derive the magnetospheric
110 convection speed, we consider 300 km/s for the anti-sunward flow speed in the magnetosheath
111 and 50 km/s for the sunward flow speed in the magnetosphere as used in previous numerical
112 studies [e.g., Seki et al., 2013; Fujimoto et al., 2007; Jia et al., 2015; Wang et al., 2010]. The
113 magnitude of the B_z magnetic field component does not vary across the magnetopause and was
114 constrained by MESSENGER data [e.g., Wang et al., 2010]. We set three different injection
115 times for ions so that we could investigate the characteristics of the ions dynamics during
116 different stages of the KH development. Illustrations of our simulation conditions are shown in
117 Figure 1. Although the figure shows only a scale of $\pm 1.0 R_M$ in the y -direction, actual
118 calculation domain is wide enough so that the gyration motions of all ions are closed within the
119 domain. In addition, although it appears visually that the development of the KH instability
120 seems to be different between the dawn and dusk side configurations studied here, we confirm
121 that the growth of the KH instability is almost the same. This behavior may be due to the initial
122 perturbation that we used this time, i.e., white noise. Although the MHD approximation may
123 not be valid especially at the dawnside magnetopause of Mercury according to previous studies
124 [e.g., Paral and Rankin, 2013], we consider in the present study both the dawn and dusk sides
125 of the magnetosphere in order to globally understand the effect of a large convection electric
126 field on the ion dynamics and transport. In addition to a configuration with a northward IMF,
127 we also consider a configuration with a southward IMF so that we could explore the physical
128 mechanisms of energization and transport of ions more thoroughly.

129 An overview of the properties of Na^+ ions for the northward IMF Case is shown in
130 Figure 2. Here 10,000 ions were injected in three different regions as picked up ions. Blue dots
131 represent individual ions in the magnetosheath, while magenta and yellow dots show individual

132 ions in the boundary layer (magnetopause) and magnetosphere region, respectively. The spatial
133 scale is normalized here by the radius of Mercury. Because the magnetopause (boundary layer)
134 is the transition layer for the physical quantities, only blue (magnetosheath) and yellow
135 (magnetosphere) dots are analyzed in this study. Initial ion positions were determined by a
136 given function and its distribution is shown in one of the right panels of Figure 2 at $t = 32.2$ [s].
137 Because of the different directions of the large-scale convection electric field between the dawn
138 and dusk sides (see left panel of Figure 2), the ion distribution during the later stage of the
139 development of the KH instability is significantly different between the dawn and dusk sides.
140 In particular, a large ion density gap can be observed near the magnetopause on the dawnside,
141 while such a gap is not seen on the duskside. Moreover, ions of magnetospheric origin (yellow
142 dots) can enter the magnetosheath region at $t = 96.6$ [s] due to the development of the KH
143 vortices on the dawnside, whereas those on the duskside could not cross the magnetopause. Still
144 on the dawnside, once ions penetrate inside the magnetosheath region, they seem to move freely
145 from the filament structure of the KH vortex. On the contrary, planetary ions picked up in the
146 magnetosheath (blue dots) did not penetrate into the magnetosphere. The situation is opposite
147 for the duskside configuration. Ions in the magnetosheath (blue dots) can enter inside the
148 magnetosphere region, whereas ions in the magnetosphere (yellow dots) penetrate less inside
149 the magnetosheath region compared to those in the case of the dawnside configuration.

150

151 **3. Results**

152 **3.1 From magnetosphere to magnetosheath**

153 Since all ions were injected as picked up ions, their initial energy depends on the energy
154 calculated from the ExB drift speed in each region. As such, the analysis and discussion should
155 be done separately. In this section, we focus on the ions picked up in the magnetosphere region
156 which are presented by yellow dots in Figure 2. Figure 3 shows the properties of Na^+ ions for

157 the case of northward IMF at given times. Although all colored dots represent Na^+ ions picked
158 up in the magnetosphere, different colors correspond to the different distances from the
159 magnetopause. Each color has an initial thickness of that of the magnetopause, $2a$. For instance,
160 the region within $\pm 0.1 R_M$ of the center of the boundary layer is defined as a magnetopause.
161 Magenta dots indicate ions initially picked up in the region $0.1 - 0.3 R_M$ from the magnetopause,
162 green dots represent the ions in the region of $0.3 - 0.5 R_M$ from the magnetopause, cyan
163 represents ions in the region of $0.5 - 0.7 R_M$ from the magnetopause, and yellow dots show the
164 ions in the region from 0.7 to $0.9 R_M$ from the magnetopause. The Na^+ ions were injected with
165 a thermal energy of 1 eV at $t = 32.2 \text{ [s]}$, corresponding to the time when the KH instability
166 begins to develop. For simplicity, we chose 90 degree of pitch angle for all ions. At $t = 128.8$
167 $[\text{s}]$, magenta and green dots on the dawnside seem to be distributed randomly and the
168 corresponding ions are transported to the magnetosheath region. On the other hand, no ions are
169 observed in the magnetosheath region on the duskside. This is because of the orientation of
170 convection electric field. At $t = 193.2 \text{ [s]}$, ions on the dawnside are distributed throughout the
171 simulation box, showing that they are well mixed. In contrast, only a fewer ions are observed
172 in the magnetosheath region on the duskside, while they are well-mixed only inside the
173 magnetosphere. The three bottom panels of Figure 3 shows, from top to bottom, the growth of
174 the KH instability, the number of energized ions, and the number of transport ions as a function
175 of time. The 2nd and 3rd panels indicate the occurrence rate, obtained by counting the number
176 of energized/transported ions and taking the ratio to the total number of ions in each region. For
177 instance, to obtain the data in the second panel, when a magenta ion is accelerated, and its
178 magnetic moment becomes $\mu/\mu_0 > 10$, it is counted as an energized ion. Next, the total number
179 of these ions is divided by the total number of ions initially injected in the magenta region. A
180 similar counting is applied for the third panel, where net transport means that an ion crosses the
181 magnetopause and is located up to a distance of $+2a$ from the magnetopause. For example, we

182 count an ion picked up in the $0.3 - 0.5 R_M$ region, colored by green for the case of the dawnside,
 183 as it crosses the magnetopause and is located above $-0.3 R_M$ in Figure 3. These rates were
 184 calculated at each computational time interval $t_{com} = 10$ (or $t = 32.2$ [s] in real time). Magenta,
 185 dark, and orange profiles in the 2nd and 3rd panels in Figure 3(b) correspond to the color dots
 186 represented in magenta and yellow, which are respectively, the closest region to and the farthest
 187 region from the magnetopause, respectively. Profiles for the properties of ions behavior colored
 188 by green and cyan are omitted here for readability.

189 Looking at Figure 3(b), we first find that non-adiabatic acceleration occurs on both the
 190 dawn and dusk sides, but ions are more significantly accelerated on the dawnside. The solid
 191 and dashed lines refer to the dawn and dusk configurations in Figure 3. For example, 85% of
 192 the ions are accelerated in the closest region to the magnetopause at dawn, while only 35% are
 193 seen at dusk. The starting time for acceleration closely matches the time of KH growth,
 194 suggesting that the formation of KH vortices efficiently accelerate ions. We point out here that
 195 ion transport here means that ions are observed in another region after crossing the
 196 magnetopause. On the dawnside, we observe ions having moved in another region only under
 197 the action of their gyration motion. We also observe ions with a large Larmor radius near the
 198 magnetopause after having crossed the magnetopause during their one of their cyclotron motion.
 199 This latter reason can lead to an oscillatory motion, which is illustrated in the bottom last panel
 200 in Figure 3(b). The fact that there is no dashed line in the 3rd panel of Figure 3(b) indicates that
 201 no transport occurs from the magnetosphere to the magnetosheath side on the duskside. We
 202 note the absence of ion transport even though the ions are energized. In the present analysis, we
 203 count all energized ions with $\mu/\mu_0 > 10$, thus some of them maybe even more energized. Ions
 204 with $\mu/\mu_0 \sim 10$ may not cross the boundary but ions with $\mu/\mu_0 \sim 100$ may do so because of their
 205 large Larmor radius and may in addition show the oscillation signature in the transport panel.
 206 To investigate this effect in more detail, we obtain the magnetic moment changes in the

207 energization and transport of ions picked up ion in the closest region to the magnetopause
208 (indicated by A and A' in Figure 3). Figure 4 shows the breakdown of energization and transport
209 of each range of the magnetic moment for the case of the closest region, as a function of time.
210 First of all, the major difference between the dusk and dawn sides in the figure is seen in the
211 energization profile. The left panel shows that energized ions have their magnetic moment
212 changing from 10 to 50 whereas profiles in the right panel show more dispersed magnetic
213 moment changes. On the duskside, 78 % of energized ions represented by the magenta profile
214 have their magnetic moment changing from 10 to 25, while the blue profile shows their
215 magnetic moment changing from 25 to 50. Figure 4 clearly shows that ions on the dawnside are
216 effectively accelerated, and the profile in the 3rd panel shows that the lower magnetic moment
217 change is also associated with some transport. The level of energization does not correspond to
218 that of transport. The question that emerges here is why do we have effective acceleration and
219 transport on the dawnside, and fewer ions are significantly energized with no transport on the
220 duskside? To address this question, we selected model trajectories to understand the dawn-dusk
221 difference of the energization and transport of planetary ions.

222 Figure 5 shows two model trajectories of picked up sodium ions in the magnetosphere
223 for both (a) dusk and (b) dawn configurations. In this figure, we selected an ion with $\mu/\mu_0 < 10$
224 at dusk as an example of limited energization and an ion with $\mu/\mu_0 > 100$ at dawn as an example
225 of efficient energization. From Top to bottom, we show the ion position in the y-direction with
226 arrows showing the electric field orientation, the electric field intensity that the ion experiences,
227 the magnetic moment which is normalized to the initial value, and energy. The electric field
228 orientation shown on the 1st panel corresponds to the direction of the Lorentz force that ion
229 experiences. For example, in Figure 5(a) at $t = 50$ [s], green arrows point towards the
230 magnetosheath side indicating that the ion is accelerated towards that side. In contrast, at $t =$
231 250 [s] in the same figure, green arrows point in the opposite direction of the electric field. At

232 this time, the ions are essentially accelerated towards the inside of the magnetosphere. Two
233 selected ions were initially injected at the same distance from the magnetopause. In figure 5(b),
234 the magnetic moment changes can be seen around the linear growth time (indicated by red
235 dashed line), and μ -jump occurred at $t \sim 115$ [s]. On the other hand, figure 5(a) does not show
236 such clear magnetic moment changes. By also checking snapshots of the properties of an ion
237 and the electric field that ion experiences, acceleration steps can be explained. At dawn, when
238 the ions is just picked up in the magnetosphere, it is subject to normal gyration motion at first.
239 The ion may experience a small electric field variation with the development of KH instability
240 and thus the ion starts the polarization drift which gradually accelerates the ion (equivalent to
241 Larmor radius increases). This is an adiabatic acceleration. When the ion enters the initial
242 boundary layer region, here at $t \sim 115$ [s], the ion suddenly experiences a large electric field
243 towards the magnetosheath where the μ -jump occurred. After that, the ion keeps its gyration
244 motion in the magnetosheath region. A model trajectory on the duskside presented in Figure
245 5(a) shows that although E burst-like signatures can be seen on the 2nd panel, the ion does not
246 gain a large amount of energy. Noting the direction of the electric field (green arrows at the 1st
247 panel), the E burst occurs when the ion moves against the electric field, and thus deceleration
248 occurs. Some ions are able to gain large energy such as the case of $\mu/\mu_0 \sim 30$ for instance, due
249 to the stronger electric field inside the rotating vortex (rotating electric field hereinafter), which
250 directs to the magnetosphere side, in the later stage of the KH development. Investigating other
251 model trajectories allow us to understand the transport of ions, which is controlled by the
252 electric field configuration in the magnetosheath under northward IMF.

253 The magnetic reconnection generally occurs during the case of southward IMF, meaning
254 that the configuration of the magnetopause will be more complicated, thus the KH instability
255 less likely occurs. However, this case presents a good example of understanding the role of the
256 large convection electric field. In this whole study, we perform the ideal MHD simulation with

257 the reversal magnetic field (from the magnetosheath to the magnetosphere, varies from - Bz to
258 + Bz) across the magnetopause with the same magnitude in the entire simulation domain. It
259 should be stressed here is that there is no magnetic reconnection so that we could have the KH
260 growth. In the dawnside configuration, we have a large electric field towards the magnetopause
261 in the magnetosheath region, while another small electric field points away from the
262 magnetopause in the magnetosphere. Conversely, in the duskside configuration, we have a large
263 electric field pointing away from the magnetopause in the magnetosheath region, and a small
264 electric field directed towards the magnetopause in the magnetosphere. As a consequence of
265 the southward IMF, ions picked up in the just adjacent region to the magnetopause, the
266 energized ratio is much higher than that of the case of northward IMF for all three heavy ion
267 species (O^+ , Na^+ , and K^+). The energized ratio increases for both dawn and dusk sides in the
268 case of southward IMF compared to the case of northward IMF. The net electric field changes
269 across the magnetopause, i.e. the electric fields in the case of northward IMF cancel each other
270 whereas they add themselves up in the case of southward IMF, resulting in an effective
271 energization in the case of southward IMF. We also investigated the breakdown of energization
272 in the same manner as for Northward Case. The breakdown contains the lower and higher
273 energized ions, and the amount of transport corresponding to the energization. In contrast, we
274 found that for highly energized ions, $\mu/\mu_0 > 100$, the energization increases in time due to the
275 rotating electric field component. On the contrary, although the magnetosheath electric field is
276 directed toward the magnetopause at dawn, the ions are transported to the magnetosheath which
277 is inconsistent with our results for the case of northward IMF. The dawnside configuration
278 under the southward IMF provides the large rotating electric field inside the KH vortex pointing
279 to the magnetosheath region, leading significant ion energization and transport in the mixing
280 region of magnetosheath side. Under a southward IMF, signatures of energization and transport
281 of ions picked up in the magnetosphere region can be seen on both the dawn and dusk sides. In

282 both cases. ions are transported and there is no stagnation inside the magnetopause. Overall,
283 ion transport starts at a later stage in the KH linear growth, being equivalent in both cases. Even
284 though the large convection electric field affects the ion transport, they cannot cross the
285 magnetopause layer without the development of the KH instability. However, in reality in the
286 magnetospheric flanks exist additional components of the magnetic field, B_x and B_y , and this
287 may lead to the effective transport of magnetospheric ions.

288

289 **3.2 From magnetosheath to magnetosphere**

290 Here we study the properties of ions picked up in the magnetosheath region. A
291 noticeable difference is the electric field which ions initially experience: ions picked up in the
292 magnetosheath imply that the ion might not experience a large E burst because of the other
293 electric field intensity affecting the ion is small compared to the electric field in the
294 magnetosheath. The results for the northward IMF case are shown in Figure 6. We can first
295 notice that non-adiabatic acceleration does not occur on both the dawn and dusk sides of the
296 magnetosphere (see 2nd panel of Figure 6(b)). Ions cannot be transported to the magnetosphere
297 on the dawnside, while moving outward from the magnetopause following the large electric
298 field in the magnetosheath. On the other hand, some ions can cross the magnetopause and move
299 inside the magnetosphere region on the duskside where they are well mixed even although they
300 are not energized. This no energization feature can be understood due to the ions initially
301 experiencing a large electric field and thus they do not experience any stronger electric field
302 during their gyration motions. Ion transport on the duskside starts at the time corresponding to
303 the linear KH growth time and its depth of penetration seems to be the same order of the fluid
304 structure represented in black and gray color, suggesting that the formation of the KH vortex
305 plays a role in the transport of ions even though they initially have a large Larmor radius.

306 Mercury's exosphere extends to a few R_M [McClintok et al., 2008] and so many ions of
307 exospheric origin can be picked up in the magnetosheath. Since these ions can have a large
308 Larmor radius (approximately of the same order or more than the magnetopause thickness),
309 these ions could penetrate inside the magnetosphere region. However, according to our results,
310 without the x and y components of the magnetic field, it is difficult to cross on the dawnside.
311 In addition, even if the ions were picked up in the duskside configuration, fewer ions were
312 transported to the magnetosphere region compared to the results in the previous section.

313 Under southward IMF, a small number of ions can be energized and some transport on
314 both the dawn and dusk sides can be seen. However, ion transport on the dawnside suddenly
315 starts when ions are injected at the beginning of the KH growth, not because of the development
316 of the KH instability but because of the effect of the large electric field itself. This leads to the
317 ion transport without KH instability. In this study, because the effect of the field variations due
318 to the development of the KH instability has been discussed, such an ion transport without the
319 KH growth should not be taken into consideration. Additional experiments were performed to
320 see ion transport without the KH growth and similar transport could be seen in the dawnside
321 configuration. In addition, we found that the ion transport without the KH growth shows no
322 large time differences even when we take into account the distance from the magnetopause. If
323 we take into account of the ion transport without the KH growth, we can conclude that small
324 (negligible) energization on both sides and ion transport on the duskside occur due to the
325 development of the KH instability. Ion energization and transport occur significantly on both
326 sides because of the same directed electric field across the magnetopause.

327

328 **3.3 Properties of lighter ion species**

329 Compared to the properties of heavy ions of planetary origin, lighter ion species that
330 were injected with initial energies of 0.047 eV (= 540 K) have different properties. Figure 7

331 shows the properties of lighter ions initially picked up in the magnetosphere for northward IMF.
332 These lighter species have a Larmor radius small enough compared to the magnetopause
333 thickness so that they can be treated as fluid, Although some ion energization can be seen after
334 the linear KH growth, no transport occurs. Our results indicate that the fine structure due to the
335 development of the KH instability causes acceleration. Although the scale of fine structures
336 cannot be characterized, it is proven by checking different species. Acceleration of hydrogen
337 ions is observed in the region closest to the magnetopause (in magenta) at $t \sim 120$ [s], whereas
338 it is observed at $t \sim 140$ [s] for protons with a smaller Larmor radius. Ion transport does not
339 occur either at dawn or dusk: it is influenced only within the expanded magnetopause (or called
340 mixing layer) due to the development of the KH instability. On the other hand, ions picked up
341 in the magnetosheath when the IMF is northward are not energized. Small transport on the
342 duskside can be observed similar to heavy ions. As we discussed previously, because the
343 rotating components of the electric field work effectively on the energization and transport of
344 ions. When the IMF is southward we found that the energization starts earlier than when the
345 IMF is northward and that significant transport can be observed at both dawn and dusk.

346 Lighter ions picked up in the magnetosheath region are also observed to be energized
347 and transported both at dawn and dusk. The main difference compared to the properties of heavy
348 ions of planetary origin is the fact that lighter ions picked up in the magnetosheath region are
349 significantly energized and transported when the IMF is southward. Indeed, because of their
350 lighter masses, it is easier for them to be trapped inside KH vortices and be affected by small
351 variations of the rotating electric field variations inside the structure.

352

353 **4. Discussion**

354 The summary tables of particle energization and transport of planetary ions for both
355 northward and southward IMF are shown in Table 2. Generally, the level of energization is

356 superior when we have southward IMF, and always in the dawnside. In particular, the
357 energization and transport of heavy ions of planetary origin picked up in the magnetosphere are
358 illustrated in Figure 8. When the IMF is northward, we found that no acceleration of heavy
359 planetary ions picked up in the magnetosheath is observed and that ion transport from the
360 magnetosphere to the magnetosheath occurs only at dawn, while a small amount of heavy ion
361 transport in the opposite direction occurs at dusk because of the electric field orientation.
362 Because of their smaller Larmor radius, lighter ions behave magnetohydrodynamically.
363 Acceleration of lighter planetary ions picked up in the magnetosphere occurs at both dawn and
364 dusk but no transport towards the magnetosheath is observed.

365 On the other hand, when the IMF is southward, the energization and transport of both
366 heavy and lighter ions initially picked up in the magnetosphere to the magnetosheath occurs at
367 both dawnside and dusks, whereas the energization of heavy ions initially picked up in the
368 magnetosheath appears negligible and there are only very little ions transported to the
369 magnetosphere, However, in this case, the heavy ion transport from the magnetosheath to the
370 magnetosphere at dawn can occur at dawn without the development of the KH instability.
371 Contrary to heavy ions, lighter planetary ions picked up in the magnetosheath can be accelerated
372 and transported due to the initial direction of the large electric field across the magnetopause.
373 Since they are light, they have a small Larmor radius and thus, they stay inside the KH vortices.
374 Those lighter ions are affected by small electric variations within the KH vortex, leading to
375 efficient acceleration and transport. In the previously described cases, we have shown only two
376 species, sodium and hydrogen ions. We now discuss the dependence on Larmor radius for the
377 ion acceleration and transport. The different properties of heavy ions compared to lighter ions
378 indicates that there is a relationship between the size of the KH vortex (equivalent to the
379 magnetopause thickness) and the Larmor radius of the ion. Figure 9 shows the dependence of
380 Larmor radius for the energization of ions picked up in the magnetosphere region, especially in

381 the region closest to the magnetopause (in magenta in previous figures), for the northward IMF.
382 The x- and y-axes are scaled by ion Larmor radius normalized to the initial half magnetopause
383 thickness and the time where the energization reaches 30% normalized to the linear growth time
384 ($t \sim 90$ [s]). The red dashed line represents $x = 1$ and $y = 1$. The circle and triangle symbols are
385 used for the duskside and dawnside cases, respectively. We performed additional calculations
386 for helium, carbon, and iron ions. According to this figure, ions are less energized at dusk
387 compared to dawn. The acceleration of lighter species take place during a late stage of the KH
388 growth, whereas ions with a larger Larmor radius, such as Fe^+ and K^+ , are accelerated just
389 after formation of the KH vortex. Though the oxygen ions seem to be accelerated effectively,
390 the Larmor radius dependence on the ion energization seems to vary gradually (see Figure 9).
391 A similar feature is observed for southward IMF. In this study, when the ions move farther than
392 the distance of $0.3 R_M$ from the magnetopause we assume they are transported to the other
393 region. However, the lighter planetary species follow the background fluid structure (MHD-
394 like) and background structure does not expand more than $0.3 R_M$ this time, they are not counted.
395 To first order, the number of planetary ions transported increases with increasing mass. For
396 example, for northward IMF 42% of carbon ions, doubly-charged iron ions and potassium ions,
397 44% of oxygen ions, and 41% of sodium ions are transported from the magnetosphere to the
398 magnetosheath at dawn, whereas in contrast none of the protons and hydrogen ions, and only
399 10% of helium ions are. For the southward IMF case, the corresponding values are 25% for
400 protons, 31% for hydrogen ions, 30% for oxygen and sodium ions, and 32% for potassium ions.
401 We may say that some threshold for MHD-like behavior can be set between helium and
402 hydrogen which can be seen in Figure 9.

403 After having discussed ion acceleration and transport within KH vortices, we now
404 discuss the possibility of solar wind plasma entry inside the magnetosphere. Two different ion
405 species, H^+ and He^{++} are included in our modeled solar wind. These ions were injected with

406 initial energies of 10 eV on the ExB frame at the simulation start time. Although H^+ can
407 originate both from the solar wind and from planetary ions, He^{++} cannot be produced in the
408 Hermean environment, and thus the detection of He^{++} can be used as a proxy for the entry of
409 solar wind plasmas inside the magnetopause. Previous results suggested that lighter ions cannot
410 be accelerated under northward IMF and that the small amount of solar wind penetration inside
411 the magnetosphere is expected because those lighter ions follow the background KH structure.
412 In addition, because we assume a proton dominant background for the MHD simulation, the 1st
413 adiabatic invariant of H^+ violation leads to the violation of the MHD approximation. Previous
414 studies on the KH instability did not discuss the limitation of the MHD approximation on the
415 nonlinear stage of the KH instability development because of its difficulty. However, when the
416 1st adiabatic invariant of H^+ is not conserved, it is a clear signature of the MHD approximation
417 violation. Here, we discuss our results for both northward and southward IMF. In both cases,
418 we consider protons picked up in the magnetosheath region closest to the magnetopause. Their
419 Larmor radius normalized to the magnetopause thickness is 0.018, whereas the Larmor radius
420 of He^{++} is ~ 0.026 . In northward IMF case, similar to the behavior of lighter ions of planetary
421 origin, solar wind plasma can also be energized within KH waves. The energized ion ratio
422 becomes almost the same and corresponds to 20% of injected ions in the closest region to the
423 magnetopause. Conversely, no ion transport was found on either side. Considering ion injection
424 time (here $t = 0$ [s]) and that acceleration happens at the same time on both the dawn and dusk
425 sides, fine structures created due to the KH vortex breaking accelerate H^+ ions. Similar
426 behavior is observed for He^{++} , where the acceleration starts at $t \sim 122$ [s]. The time delay of
427 the energization start for protons is reasonably understood because they have twice smaller
428 different Larmor radius compared to that of He^{++} . Negligible ion transport has been observed
429 at $t \sim 130$ [s] for protons, and their transport starts before the acceleration starts. This transport
430 is understood as MHD-like transport, as the proton motion seems to follow the motion of fluid

431 background proton. In addition, the Larmor radius of He^{++} is large enough not to follow the
432 fluid background. On the other hand, in Southward Case, both He^{++} and H^+ show
433 qualitatively similar results. Ion energization and transport can be seen on both sides. The ion
434 energization starts at $t \sim 110$ [s] for H^+ and $t \sim 108$ [s] for He^{++} . Moreover, ion transport
435 starts at $t \sim 120$ [s] for H^+ and $t \sim 120$ [s] for He^{++} in contrast to Northward Case. Ion
436 acceleration occurs both on the dawn and dusk sides with almost the same ratio, with ion
437 transport being more effective on the duskside. In addition, ion transport in Southward Case
438 starts at the same time as energization starts. This suggests that ions can be transported due to
439 acceleration from the rotational components of the electric field inside the KH vortex in the
440 same manner as for ions of planetary origin. Those results are summarized in Table 3. At same
441 time, the 1st adiabatic moment of a proton at $t = 145$ [s], for Northward Case, indicates that the
442 MHD approximation is not valid anymore. Though our injected proton had different
443 characteristics as the background proton had, it implies that we need to consider the ion kinetics
444 at a later stage of the KH non-linear phase. In this study, we do not focus on this, however this
445 aspect could be studied in the future. Is it possible to have a solar wind plasma entry through a
446 KH vortex? Our results suggest that the ions can be transported magnetohydrodynamically,
447 meaning that the size of the solar wind plasma entry region is determined by the vortex size.
448 Especially, even if we do not have any magnetic reconnections, solar wind plasmas are subject
449 to enter into the magnetosphere region during southwards IMF due to the convection electric
450 field.

451 Combining all these results, we can show that the ions on the dawnside are less dense
452 than the ions on the duskside under a northward IMF. Indeed, on the duskside, ions picked up
453 in the magnetosphere cannot cross the magnetopause, and those in the magnetosheath can
454 penetrate inside the magnetosphere. In order to be accelerated by variations of the electric field,
455 the ions should be inside the magnetopause where the initial electric field is smaller than that

456 in the other region. Moreover, the energized and transported ratio in both sides is leveling off
457 in Figure 3 for instance, 85% (35%) of the energized ratio at dawn (dusk) in the closest region.
458 This seems to indicate that heavy ions are not affected by small-scale structures (so-called fine
459 structures) due to the breaking of KH vortices in the non-linear growth (saturation) phase of the
460 instability but we note that there fine structures have an effect on the acceleration of lighter
461 ions that have smaller Larmor radius.

462

463 **5. Conclusions**

464 Particle trajectory computations have been performed in a time-varying MHD model of
465 KH vortices in order to understand the properties of ions within KH vortices. First of all, we
466 revealed that the large-scale convection electric field plays an important role for the ion
467 acceleration and transport. The results from both Northward and Southward cases showed that
468 the ion transport is well controlled by the electric field orientation in the magnetosheath having
469 a stronger electric field. Ions picked up in the magnetosphere are energized on both the dawn
470 and dusk sides under both northward and southward IMF. In particular, we found when the IMF
471 is southward that ions are efficiently accelerated within KH vortices due to the developed
472 electric field orientation inside the vortex. Regarding lighter ions, including the solar wind
473 plasmas, their Larmor radius is small enough compared to the magnetopause thickness and thus
474 small enough not to be accelerated during the linear growth phase of the KH instability,
475 resulting in the MHD-like behavior. In their non-linear stage, KH vortices start to break and
476 make fine structures, whose scale becomes comparable to the Larmor radius. Ions can be
477 energized with these fine structures. Non-adiabatic energization of solar wind protons goes
478 beyond the limitation of MHD validation. In the later stage of the nonlinear phase, the ion
479 kinetics should be taken into account for physics. In this study, although we did not consider
480 any parallel component of the magnetic field to the wavenumber of KH and the existence of

481 ions already moving non-adiabatically, some general features should be detected by instruments
482 aboard a spacecraft. First, energized ions in the magnetosphere region on both the dawn and
483 dusk sides with the development of the KH instability are an important feature. If we have a
484 wide range of plasma ion analyzer from a few eV to keV, ion acceleration should be observed
485 and thus, the energy distribution would be changed between the KH and non-KH events. The
486 FIPS instrument onboard MESSENGER had an energy range from 100 eV/e to 13 keV/e and,
487 therefore, was too limited to identify the acceleration process for picked up ions. The
488 BepiColombo mission now en route to Mercury includes a full set of more sophisticated
489 charged particle instruments. In particular, the MSA instrument onboard the MIO spacecraft
490 has a wider energy range that can cover the picked up ion acceleration theoretically found in
491 this study, and with a wider FOV will be used for a better understanding of this non-adiabatic
492 energization and transport within KH vortices at Mercury.

493

494 **Acknowledgments.** The work of S. Aizawa was supported by the International Joint Graduate
495 Program in Earth and Environmental Sciences (GP-EES). The method used in this study is
496 referred to properly in the reference (e.g., Aizawa et al., 2018). Simulation data used in this
497 study is available in the link:

498 http://rosina1.irap.omp.eu/documents/PUBLICATIONS/AIZAWA/AIZAWA2020_PSS/.

499

500

501

502

503

504

505

506

507

508

509

510

511

512

513

514

515

516

517

518

519

520

521

522

523

524

525

526

527

528

529

530 **REFERENCES**

531

532 Aizawa, S., D. Delcourt, and N. Terada (2018), Sodium ion dynamics in the magnetospheric flanks of
533 Mercury, *Geophys. Res. Lett.*, 45(2), 595–601, doi:10.1002/2017GL076586.

534 Boardsen, S. A., T. Sundberg, J. A. Slavin, B. J. Anderson, H. Korth, S. C. Solomon, and L. G.
535 Blomberg (2010), Observations of Kelvin-Helmholtz waves along the dusk-side boundary of
536 Mercury's magnetosphere during MESSENGER's third flyby, *Geophys. Res. Lett.*, 37, L12101,
537 doi:10.1029/2010GL043606.

538 Delcourt, D. C., S. Grimald, F. Leblanc, J. -J. Berthelier, A. Millilo, A. Mura, S. Orsini, and T. E. Moore
539 (2003), A quantitative model of the planetary Na⁺ contribution to Mercury's magnetosphere, *Ann.*
540 *Geophys.*, 21, 1723–1736, doi:10.5194/angeo-21-1723-2003.

541 Dewey, R. M., Slavin, J. A., Raines, J. M., Baker, D. N., & Lawrence, D. J. (2017). Energetic electron
542 acceleration and injection during dipolarization events in Mercury's magnetotail. *Journal of*
543 *Geophysical Research: Space Physics*, 122, 12,170–12,188. <https://doi.org/10.1002/2017JA024617>

544 Dewey, R. M., Raines, J. M., Sun, W., Slavin, J. A., & Poh, G. (2018). MESSENGER observations of
545 fast plasma flows in Mercury's magnetotail. *Geophysical Research Letters*, 45, 10,110–10,118.
546 <https://doi.org/10.1029/2018GL079056>

547 DiBraccio, G. A., J. A. Slavin, S. A. Boardsen, B. J. Anderson, H. Korth, T. H. Zurbuchen, J. M.
548 Raines, D. N. Baker, R. L. McNutt Jr., and S. C. Solomon (2013), MESSENGER observations of
549 magnetopause structure and dynamics at Mercury, *J. Geophys. Res.*, 118(3), 997–1008,
550 doi:10.1002/jgra.50123.

551 Fujimoto, M., W. Baumjohann, K. Kabin, R. Nakamura, J. A. Slavin, N. Terada, and L. Zelenyi (2007),
552 Hermean magnetosphere-solar wind interaction, *Space Sci. Rev.*, 132(2–4), 529–550,
553 doi:10.1007/s11214-007-9245-8.

554 Gershman, D. J., J. M. Raines, J. A. Slavin, T. H. Zurbuchen, T. Sundberg, S. A. Boardsen, B. J.
555 Anderson, H. Korth, and S. C. Solomon (2015), MESSENGER observations of multiscale Kelvin-
556 Helmholtz vortices at Mercury, *J. Geophys. Res.*, *120*(6), 4354–4368, doi:10.1002/2014JA020903.

557 Gingell, P. W., T. Sundberg, and D. Burgess (2015), The impact of a hot sodium ion population on the
558 growth of the Kelvin-Helmholtz instability in Mercury’s magnetotail, *J. Geophys. Res.*, *120*(7), 5432–
559 5442, doi:10.1002/2015JA021433.

560 Imber, S. M., J. A. Slavin, S. A. Boardsen, B. J. Anderson, H. Korth, R. L. McNutt Jr., and S. C.
561 Solomon (2014), MESSENGER observations of large dayside flux transfer events: Do they drive
562 Mercury’s substorm cycle?, *J. Geophys. Res. Space Physics*, *119*, 5613–5623, doi:10.1002/
563 2014JA019884.

564 Imber, S. M., & Slavin, J. A. (2017). MESSENGER observations of magneto- tail loading and
565 unloading: Implications for substorms at Mercury. *Journal of Geophysical Research: Space Physics*,
566 *122*, 11,402–11,412. <https://doi.org/10.1002/2017JA024332>

567 Jia, X., J. A. Slavin, T. I. Gombosi, L. K. S. Daldorff, G. Toth, and B. van der Holst (2015), Global
568 MHD simulations of Mercury’s magnetosphere with coupled planetary interior: Induction effect of the
569 planetary conducting core on the global interaction, *J. Geophys. Res.*, *120*(6), 4763–4775,
570 doi:10.1002/2015JA021143.

571 Liljeblad, E., T. Sundberg, T. Karlsson, and A. Kullen (2014), Statistical investigation of Kelvin-
572 Helmholtz waves at the magnetopause of Mercury, *J. Geophys. Res.*, *119*(12), 9670–9683,
573 doi:10.1002/2014JA020614.

574 Liljeblad, E., T. Karlsson, T. Sundberg, and A. Kullen (2016), Observations of magnetospheric ULF
575 waves in connection with the Kelvin-Helmholtz instability at Mercury, *J. Geophys. Res.*, *121*(9), 8576–
576 8588, doi:10.1002/2016JA023015.

577 McClintock, W. E., E. T. Bradley, R. J. Vervack Jr., R. M. Killen, A. L. Sprague, N. R. Izenberg, and
578 S. C. Solomon (2008), Mercury's exosphere: Observations during MESSENGER's first Mercury
579 flyby, *Science*, 321(5885), 92–94, doi:10.1126/science.1159467.

580 Paral, J., and R. Rankin (2013), Dawn-dusk asymmetry in the Kelvin-Helmholtz instability at Mercury,
581 *Nat. Commun.*, 4, 1645, doi:10.1038/Ncomms2676.

582 Raines, J. M., J. A. Slavin, T. H. Zurbuchen, G. Gloeckler, B. J. Anderson, D. N. Baker, H. Korth, S.
583 M. Krimigis, and R. L. McNutt Jr. (2011), MESSENGER observations of the plasma environment
584 near Mercury, *Planet. Space Sci.*, 59(15), 2004–2015, doi:10.1016/j.pss.2011.02.004.

585

586 Raines, J. M., D. J. Gershman, T. H. Zurbuchen, M. Sarantos, J. A. Slavin, J. A. Gilbert, H. Korth, B.
587 J. Anderson, G. Gloeckler, S. M. Krimigis, D. N. Baker, R. L. McNutt Jr., and S. C. Solomon (2013),
588 Distribution and compositional variations of plasma ions in Mercury's space environment: The first
589 three Mercury years of MESSENGER observations, *J. Geophys. Res.*, 118(4), 1604–1619,
590 doi:10.1029/2012JA018073.

591 Schriver, D., P. M. Trávníček, B. J. Anderson, M. Ashour-Abdalla, D. N. Baker, M. Benna, S. A.
592 Boardsen, R. E. Gold, P. Hellinger, G. C. Ho, H. Korth, S. M. Krimigis, R. L. McNutt Jr., J. M.
593 Raines, R. L. Richard, J. A. Slavin, S. C. Solomon, R. D. Starr, and T. H. Zurbuchen (2011a), Quasi-
594 trapped ion and electron populations at Mercury, *Geophys. Res. Lett.*, 38(23), L23103,
595 doi:10.1029/2011GL049629.

596 Schriver, D., P. M. Trávníček, M. Ashour-Abdalla, R. L. Richard, P. Hellinger, J. A. Slavin, B. J.
597 Anderson, D. N. Baker, M. Benna, S. A. Boardsen, R. E. Gold, G. C. Ho, H. Korth, S. M. Krimigis,
598 W. E. McClintock, J. L. McLain, T. M. Orlando, M. Sarantos, A. L. Spragur, R. D. Starr, (2011b),
599 Electron transport and precipitation at Mercury during the MESSENGER flybys: Implications for
600 electron-stimulated desorption, *Planet. Space Sci.*, 59(15), 2026-2036, doi:10.1016/j.pss.2011.03.008.

601 Seki, K., N. Terada, M. Yagi, D. C. Delcourt, F. Leblanc, and T. Ogino (2013), Effects of the surface
602 conductivity and the IMF strength on the dynamics of planetary ions in Mercury's magnetosphere, *J.*
603 *Geophys. Res.*, *118*(6), 3233–3242, doi:10.1002/jgra.50181.

604 Siscoe, G. L., N. F. Ness, and C. M. Yeates (1975), Substorms on Mercury?, *J. Geophys. Res.*, *80*(31),
605 4359–4363, doi:10.1029/JA080i031p04359.

606 Slavin, J. A., et al. (2009), MESSENGER observations of Mercury's magnetosphere during northward
607 IMF, *Geophys. Res. Lett.*, *36*, L02101, doi:10.1029/2008GL036158.

608 Slavin, J. A., B. J. Anderson, D. N. Baker, M. Benna, S. A. Boardsen, G. Gloeckler, R. E. Gold, G. C.
609 Ho, H. Korth, S. M. Krimigis, R. L. McNutt Jr., L. R. Nittler, J. M. Raines, M. Sarantos, D. Schriver,
610 S. C. Solomon, R. D. Starr, P. M. Trávníček, and T. H. Zurbuchen (2010a), MESSENGER
611 observations of extreme loading and unloading of Mercury's magnetic tail, *Science*, *329*(5992), 665–
612 668, doi:10.1126/science.1188067.

613 Slavin, J. A., R. P. Lepping, C. -C. Wu, B. J. Anderson, D. N. Baker, M. Benna, S. A. Boardsen, R. M.
614 Killen, H. Korth, S. M. Krimigis, W. E. McClintock, R. L. McNutt Jr., M. Sarantos, D. Schriver, S. C.
615 Solomon, P. Trávníček and T. H. Zurbuchen (2010b), MESSENGER observations of large flux
616 transfer events at Mercury, *Geophys. Res. Lett.*, *37*(2), L02105, doi:10.1029/2009GL041485.

617 Slavin, J. A., G. A. DiBraccio, D. J. Gershman, S. M. Imber, G. K. Poh, J. M. Raines, T. H.
618 Zurbuchen, X. Jia, D. N. Baker, K. -H. Glassmeier, S. A. Livi, S. A. Boardsen, T. A. Cassidy, M.
619 Sarantos, T. Sundberg, A. Masters, C. L. Johnson, R. M. Winslow, B. J. Anderson, H. Korth, R. L.
620 McNutt Jr., and S. C. Solomon (2014), MESSENGER observations of Mercury's dayside
621 magnetosphere under extreme solar wind conditions, *J. Geophys. Res.*, *119*(10), 8087–8116,
622 doi:10.1002/2014JA020319.

623 Shue, J.-H., J. K. Chao, H. C. Fu, C. T. Russell, P. Song, K. K. Khurana, and H. J. Singer (1997), A new
624 functional form to study the solar wind control of the magnetopause size and shape, *J. Geophys. Res.*,
625 102, 9497–9511, doi:10.1029/97JA00196.

626 Sundberg, T., S. A. Boardsen, J. A. Slavin, L. G. Blomberg, J. A. Cumnock, S. C. Solomon, B. J.
627 Anderson, and H. Korth (2011), Reconstruction of propagating Kelvin-Helmholtz vortices at Mercury's
628 magnetopause, *Planet. Space Sci.*, 59(15), 2051–2057, doi:10.1016/j.pss.2011.05.008.

629 Sundberg, T., S. A. Boardsen, B. J. Anderson, H. Korth, G. C. Ho, D. Schriver, V. M. Uritsky, T. H.
630 Zurbuchen, J. M. Raines, D. N. Baker, S. M. Krimigis, R. L. McNutt Jr., and S. C. Solomon (2012a),
631 MESSENGER observations of dipolarization events in Mercury's magnetotail, *J. Geophys. Res.*,
632 117(A12), A00M03, doi:10.1029/2012JA017756.

633 Sundberg, T., S. A. Boardsen, J. A. Slavin, B. J. Anderson, H. Korth, T. H. Zurbuchen, J. M. Raines,
634 and S. C. Solomon (2012b), MESSENGER orbital observations of large-amplitude Kelvin- Helmholtz
635 waves at Mercury's magnetopause, *J. Geophys. Res.*, 117(A4), A04216, doi:10.1029/2011JA017268.

636 Wang, Y. -C., J. Mueller, U. Motschmann, and W. -H. Ip (2010), A hybrid simulation of Mercury's
637 magnetosphere for the MESSENGER encounters in year 2008, *Icarus*, 209(1), 46–52,
638 doi:10.1016/j.icarus.2010.05.020.

639 Winslow, R. M., Anderson, B. J., Johnson, C. L., Slavin, J. A., Korth, H., Purucker, M. E., Baker, D.
640 N., and Solomon, S. C. (2013), Mercury's magnetopause and bow shock from MESSENGER
641 Magnetometer observations, *J. Geophys. Res. Space Physics*, 118, 2213–2227, doi:10.1002/jgra.50237.

642 Zurbuchen, T. H., J. M. Raines, G. Gloeckler, S. M. Krimigis, J. A. Slavin, P. L. Koehn, R. M. Killen,
643 A. L. Sprague, R. L. McNutt Jr., and S. C. Solomon (2008), MESSENGER observations of the
644 composition of Mercury's ionized exosphere and plasma environment, *Science*, 321(5885), 90–92,
645 doi:10.1126/science.1159314.

646 Zurbuchen, T. H., J. M. Raines, J. A. Slavin, D. J. Gershman, J. A. Gilbert, G. Gloeckler, B. J.
647 Anderson, D. N. Baker, H. Korth, S. M. Krimigis, M. Sarantos, D. Schriver, R. L. McNutt Jr., and S.
648 C. Solomon (2011), MESSENGER observations of the spatial distribution of planetary ions near
649 Mercury, *Science*, 333(6051), 1862–1865, doi:10.1126/science.1211302.

650

651

652 **Table 1.** Summary of Parameter settings

region	Magnetosheath (MSH)	Magnetosphere (MSP)
Background H ⁺ number density	100 ions/cc	10 ions/cc
Flow velocity (MSO)	- 300 km/s	+ 50 km/s
Injected Planetary ion species (m/q)	H ⁺ (1), H ^½ (2), O ⁺ (16), Na ⁺ (23), K ⁺ (39)	
Solar wind plasma in ExB frame (m/q)	H ⁺ (1), He ⁺⁺ (2)	
Initial particle energy	H ⁺ (1), H ^½ (2) : 0.047 eV (540K) in Mercury frame	
	O ⁺ (16), Na ⁺ (23), K ⁺ (39) : 1 eV in Mercury frame	
	H ⁺ (1), He ⁺⁺ (2) : 10 eV in ExB frame	
Injection time	32.2 s, 80.5 s, 128.8 s	
Magnetic field (Bz)	+/- 48.7 nT	+ 48.7 nT

653

654 **Case**

	IMF (Bz)	Magnetopause thickness	KH wavelength
Northward IMF	+ 48.7 nT	515 km	1.5 R _M
Southward IMF	- 48.7 nT	515 km	1.5 R _M

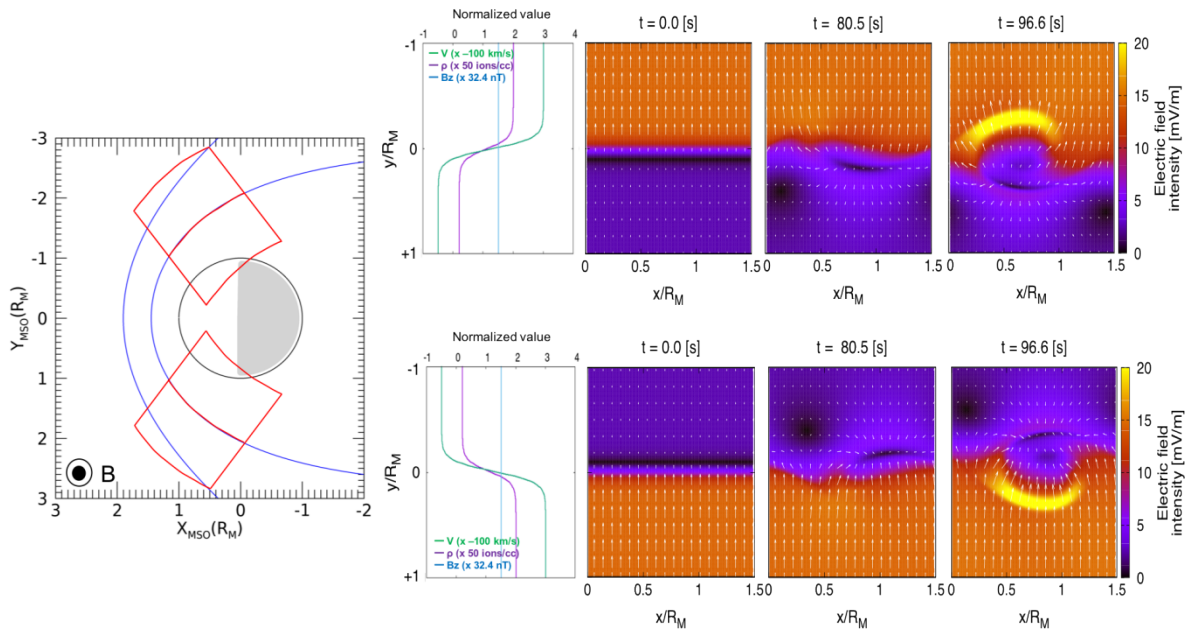
655

656

657

658

659



660

661 **Fig 1.** Illustration of simulation conditions for the case of Northward IMF.

662 The left panel shows the location of the bow shock (BS) and magnetopause (MP) from models
 663 by Slavin et al. (2009) for BS and Shue et al. (1997) for MP in MSO coordinates, respectively.

664 The parameters for those paraboloid are taken from Winslow et al. (2013). The two red boxes
 665 delineate the area of the KH occurrence on both flanks of the magnetosphere of Mercury and,
 666 therefore, our simulation domain. Initial profiles of normalized physical quantities and color-

667 coded electric field intensity obtained from MHD modeling are shown on the right panel. White
 668 arrows indicate the electric field orientation. The upper and lower color-coded panels

669 correspond to electric field maps at distinct simulation times during the evolution of the KH
 670 instability on the dawn and dusk sides, respectively. Here we assumed that the solar wind is

671 flowing tailward with a velocity of 300 km/s and that the magnetospheric convection flows
 672 from the nightside to the dayside with a velocity of 50 km/s. Initial variations of physical

673 quantities across the magnetopause follow hyperbolic tangent profiles. The thickness of the

674 magnetopause is 515 km and the wavelength of the KH instability is set to $1.5 R_M$ km, which
 675 is consistent with MESSENGER observations.

676

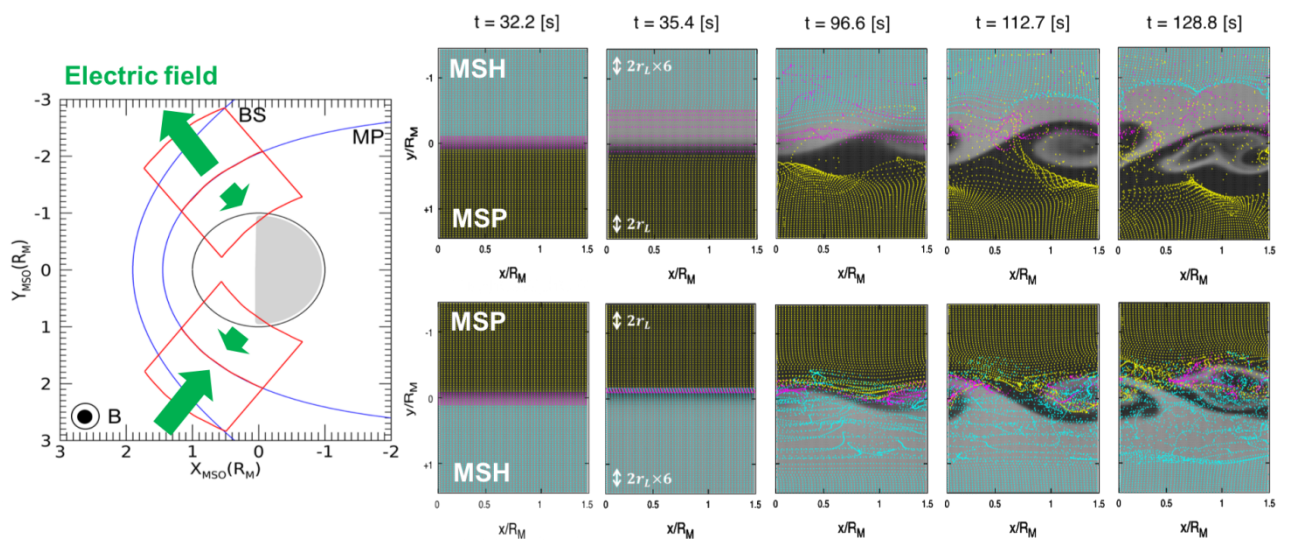
677

678

679

680

681



682

683

684 **Fig 2.** Properties of sodium ions at distinct simulation times during the development of the KH
 685 instability for the case of Northward IMF. Background grey scale color shows the proton
 686 number density (light (dark) colors indicate higher (lower) density). Yellow, magenta and cyan
 687 dots represent sodium ions picked up in the magnetosphere, magnetopause (boundary layer),
 688 and magnetosheath regions, respectively. The upper and lower panels show the dawn and dusk
 689 side configurations and the white arrows in the panels at $t = 35.4$ [s] indicate the Larmor radii
 690 of the sodium ions in each region. The electric field orientation and intensity is given in the left

691 panel. Each ion is injected with an initial thermal energy of 1 eV as a picked up ion at $t = 32.2$
692 [s], which corresponds to the beginning of the KH growth.

693

694

695

696

697

698

699

700

701

702

703

704

705

706

707

708

709

710

711

712

713

714

715

716

717

718

719

720

721

722

723

724

725

726

727

728

729

730

731

732

733

734

735

736

737

738

739

740

741
742
743
744
745
746
747
748
749
750
751
752
753
754
755
756
757
758
759
760
761
762
763
764
765

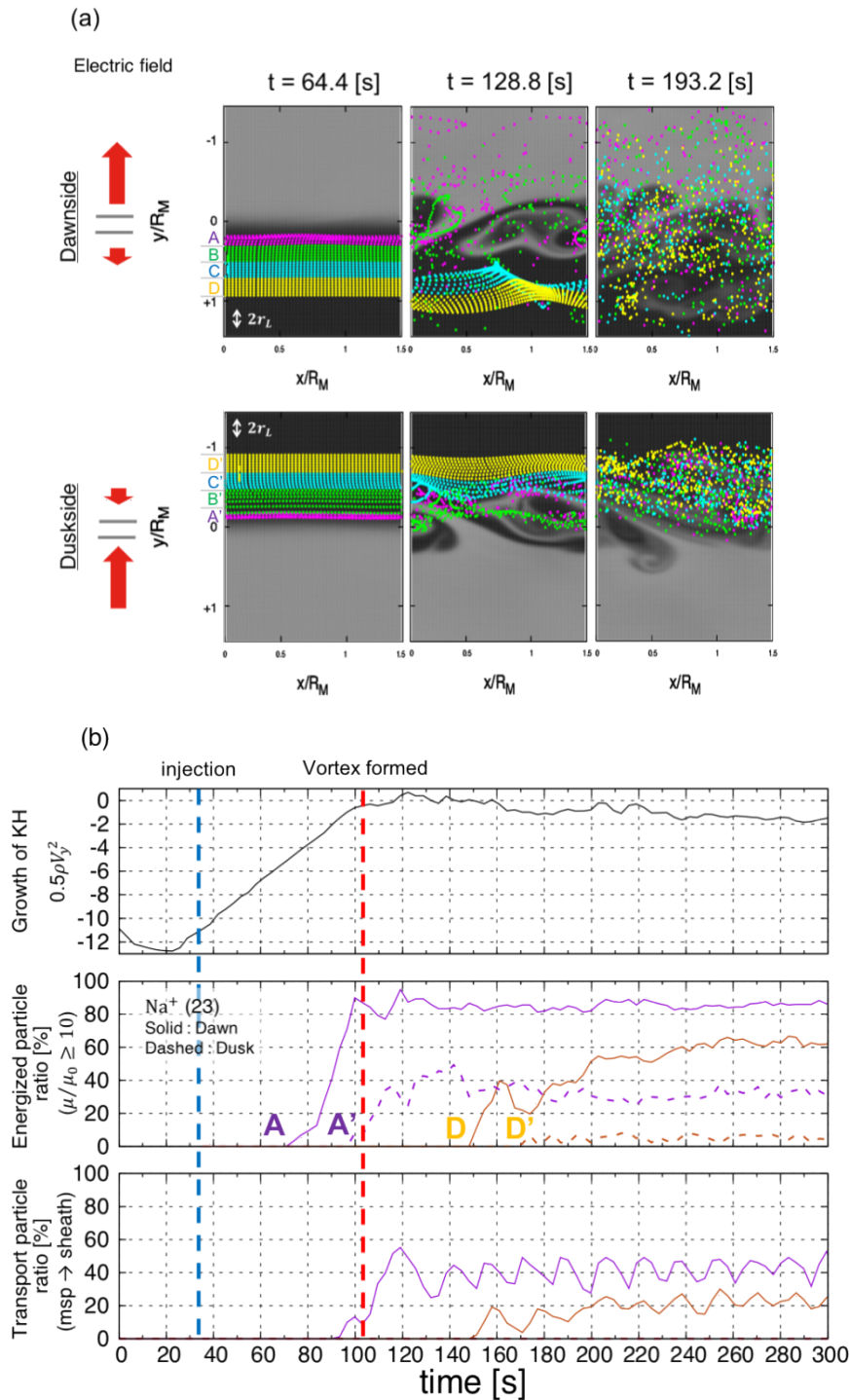
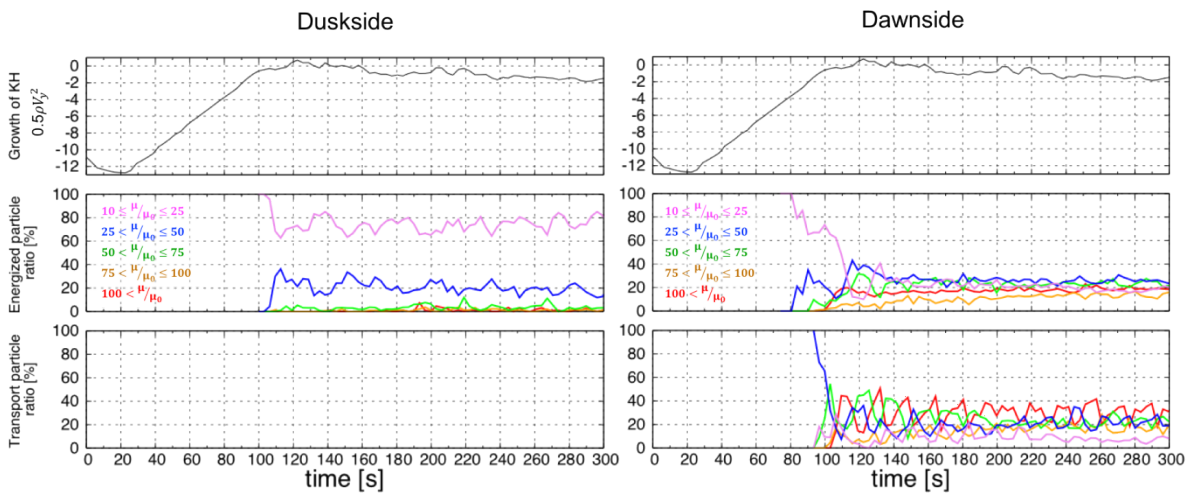


Fig 3. Energization and transport of sodium ions picked up in the magnetosphere. (a) Colored panels in the upper part of the figure represent snapshots of the properties of sodium ions at a given time in the dawn

(top) and dusk (bottom) configuration. The region in magenta (indicated by A and A') is the closest region to the magnetopause whereas the region in yellow (indicated by D and D') is the farthest region from the magnetopause. Each region has the same thickness as the magnetopause, i.e. $2a$. The white arrows indicate the Larmor radii of sodium ions at the time of injection. The initial direction of the electric field for each field configuration is given on the left. (b) The top

766 to bottom panels show the time series of the peak vertical kinetic energy as a proxy for the KH
767 growth, the ratio of energized ions ($\mu/\mu_0 > 10$) to the total number of ions in each region, and
768 the ratio of transported ions that entered the magnetosheath region ($y > -0.3 R_M$ at dawn and y
769 $> +0.3 R_M$ at dusk) to the total number of ions in each region. The magenta and yellow line
770 profiles refer to ions originating from the regions A, A' and D, D' in Fig. 3a, respectively. Solid
771 and dashed lines in the 2nd and 3rd panels are used for the dawn and dusk sides, respectively.
772 The vertical red dashed line shows the linear growth time of the KH. All ions are injected at t
773 $= 32.2$ [s] (the vertical blue dashed line) with an initial thermal energy of 1 eV.

774
775
776
777



778
779

780 Figure 4. Breakdown of ion energization and transport for ions initially picked up in the
781 magnetosphere in the case of Northward IMF. The left (right) panel shows the results on the
782 duskside (dawnside). Each colored line corresponds to a change in the magnetic moment of the
783 ions. The red line shows ions energized with $\mu/\mu_0 > 100$, the orange line is for ions with

784 magnetic moment in the range of $75 < \mu/\mu_0 \leq 100$, the green line is for ions with magnetic
 785 moment in the range of $50 < \mu/\mu_0 \leq 75$, the blue line is for ions with magnetic moment in the
 786 range of $25 < \mu/\mu_0 \leq 50$, and the magenta line is for ions with magnetic moment in the range
 787 of $10 \leq \mu/\mu_0 \leq 25$.

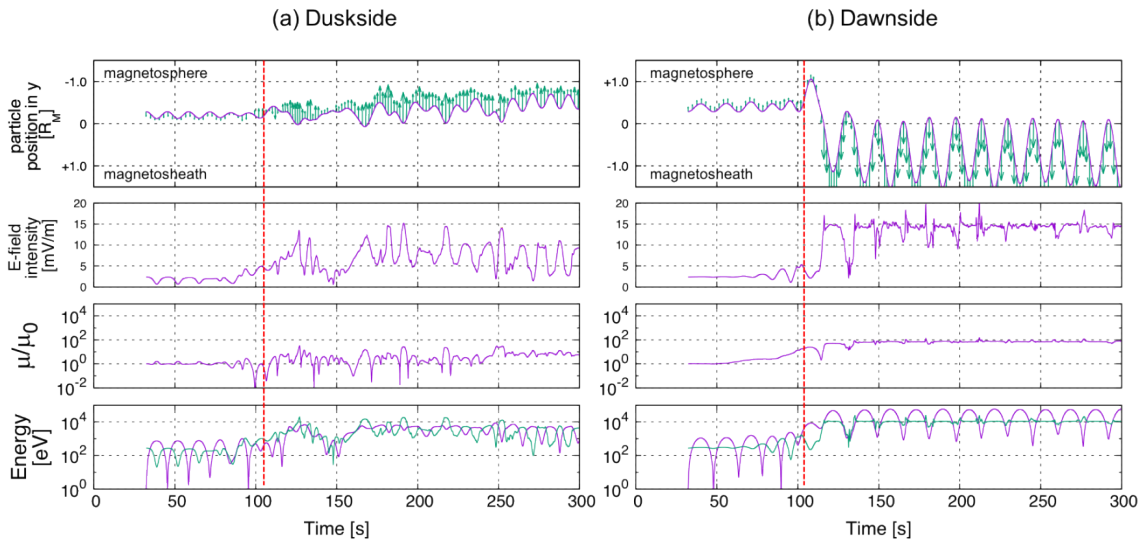
788

789

790

791

792



793

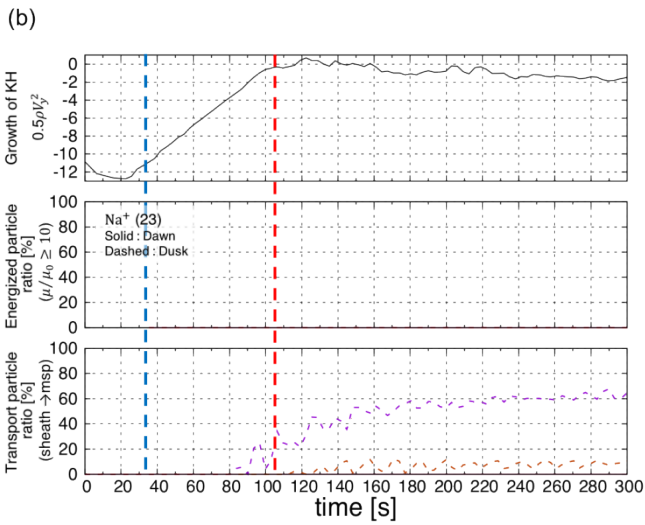
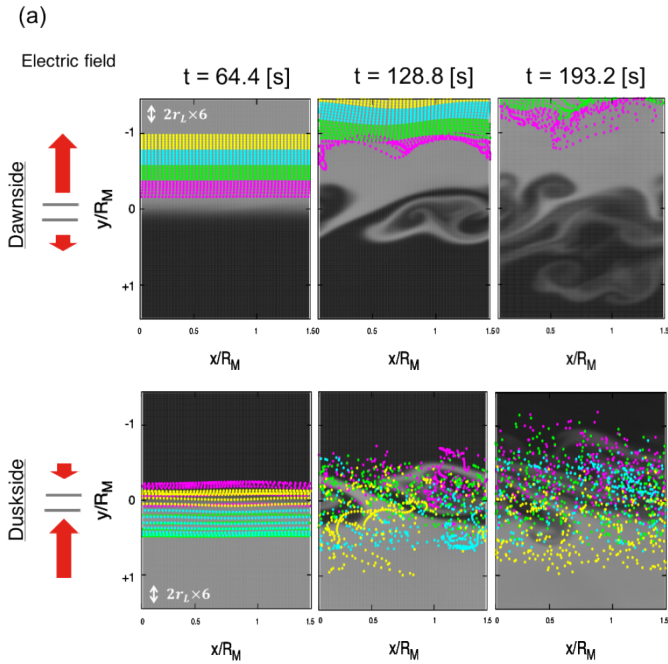
794

795 Figure 5. Model trajectories at (a) dusk and (b) dawn. The red dashed line represents the linear
 796 growth time of the KH instability. From top to bottom, each panel shows the ion position in the
 797 y-direction with the electric field orientation (green arrows), the electric field intensity, the
 798 magnetic moment (normalized to the initial value), and the energy as a function of time.

799

800

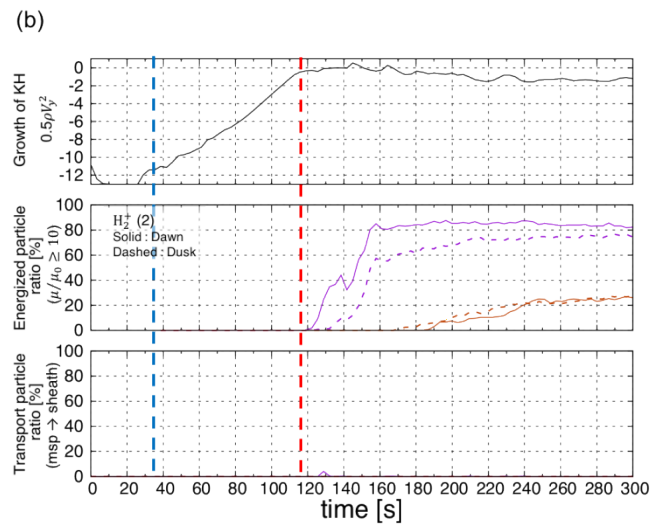
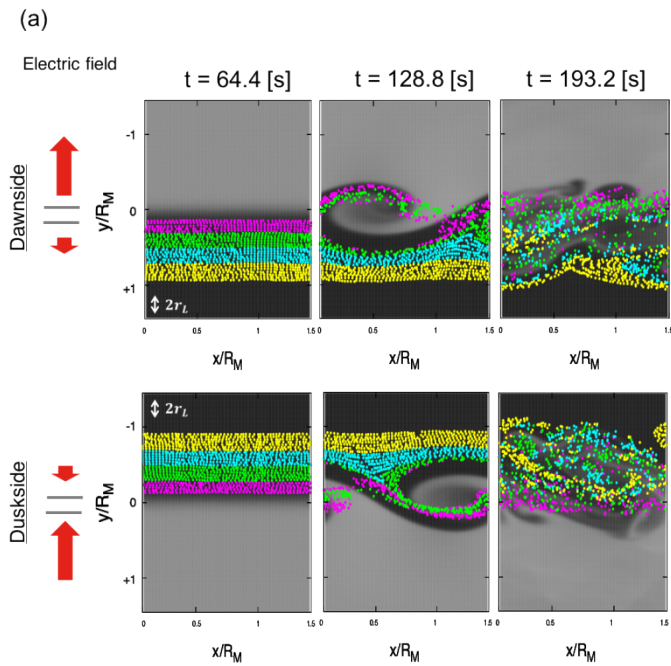
801



802

803 Figure 6. Energization and transport of sodium ions picked up in the magnetosheath. Same
804 format as the one used in Figure 3 except that transported ions now move in the opposite
805 direction.

806 .



807

808 Figure 7. Energization and transport of hydrogen ions picked up in the magnetosphere. Same
 809 format as the one used in Figure 3.

810

811

812

813

814

815
 816
 817
 818
 819
 820
 821
 822
 823
 824
 825
 826

(a) Northward IMF Case

IMF +Bz	Picked up in		dawn	dusk	comment
energization	MSH	h	×	×	
		l	×	×	MHD-like
	MSP	h	⊙	○	
		l	⊙	○	MHD-like
transport	MSH → MSP	h	×	○*	* transport can occur due to convection electric field
		l	×	△*	
	MSP → MSH	h	○	×	
		l	×	×	

827
 828
 829

830 (b) Southward IMF Case

IMF -Bz	Picked up in		dawn	dusk	comment
energization	MSH	h	△	△	negligible
		l	○	○	
	MSP	h	⊙	⊙	
		l	⊙	⊙	
transport	MSH → MSP	h	○*	○	* transport can occur due to convection electric field
		l	○	○	
	MSP → MSH	h	○	○	
		l	○	○	

831

832

833 Table 2. Summary tables for the energization and transport of planetary ions (h for heavy
 834 ions, l for light ions) in the closest region to the magnetopause. (a) and (b) show the
 835 northward and southward IMF case, respectively. Each symbol, double circle, circle, and
 836 triangle indicates the level of energization and transport. A double circle is used when the
 837 level of energization (transport) is higher than 80%, whereas a triangle is used when those are
 838 lower than 20%. A circle represents its level between 20 – 80 %.

839

840

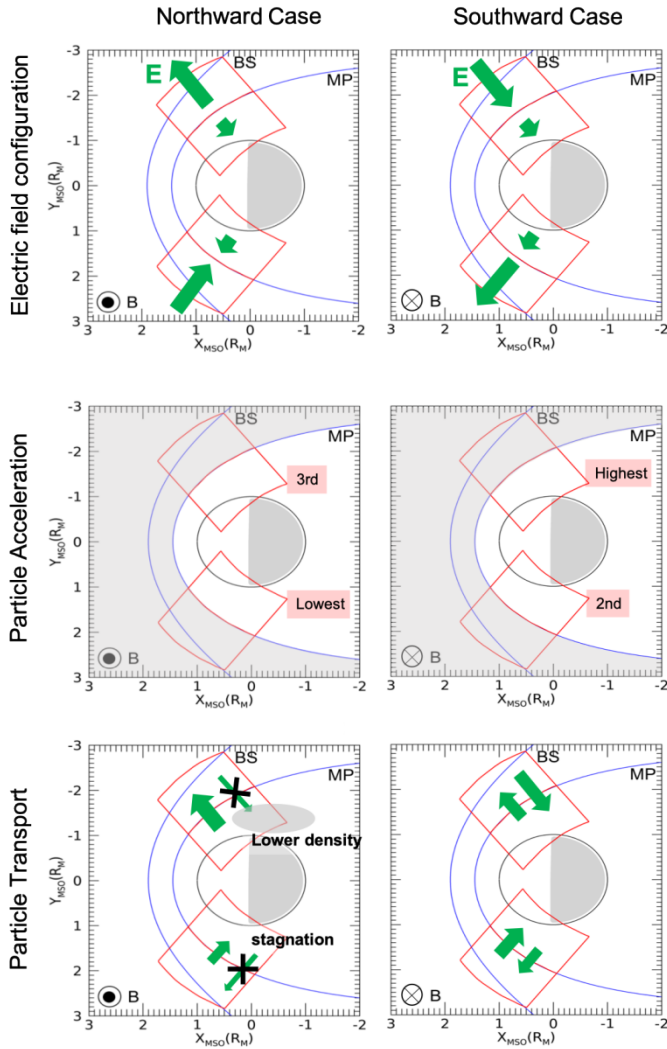
841

842

843

844

845



846

847

848 Figure 8. Illustration of general features of ion energization and transport of heavy ions of
849 planetary origin (O^+ , Na^+ , and K^+ in this study) for north and southward IMF cases. From
850 top to bottom, each panel shows the initial large electric field configuration, ion acceleration,
851 and ion transport in the x-y plane. The grey hashed area in the ion acceleration panel shows no
852 energization.

853

854

855

856

857

858

859

860

861

862

863

864

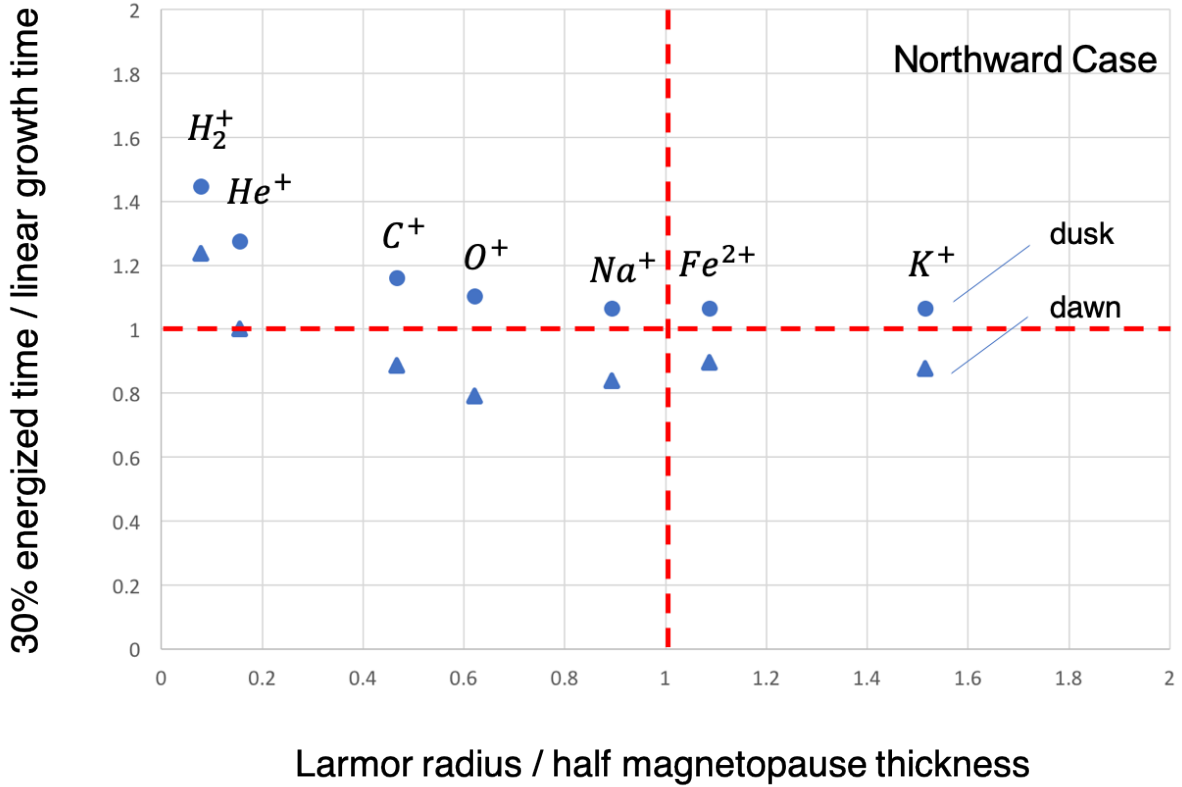
865

866

867

868

869



870

871 Figure 9. Larmor radius dependence on the ion energization of ions picked up in the
 872 magnetosphere, which is the region closest to the magnetopause under the northward IMF. The
 873 area below the horizontal red dashed line corresponds to the linear growth stage and the area
 874 above is nonlinear growth phase of the development of the KH instability.

875

876

877

878

	Region	IMF Bz	dawn	dusk	comment
Energization	MSH	+	⊙	⊙	

		-	⊙	⊙	
Transport	MSH → MSP	+	×	×	MHD-like
		-	○	○	MHD-like

879

880 Table 3. The summary tables of energization and transport of solar wind.

881

882

Declaration of interests

The authors declare that they have no known competing financial interests or personal relationships that could have appeared to influence the work reported in this paper.

The authors declare the following financial interests/personal relationships which may be considered as potential competing interests: